

# In-plane and out-of-plane magnetoresistivity in a MTG Er-doped YBCO crystal

T Yang<sup>1</sup>, Z H Wang<sup>1</sup>, H Zhang<sup>2</sup>, Y Nie<sup>1</sup>, J Fang<sup>3</sup>, H Luo<sup>1</sup>, X F Wu<sup>1</sup> and S Y Ding<sup>1</sup>

<sup>1</sup> Department of Physics and National Laboratory of Solid State Microstructures, Nanjing University, Nanjing 210093, People's Republic of China

<sup>2</sup> Shanghai Institute of Metallurgy, Chinese Academy of Sciences, Shanghai 200050, People's Republic of China

<sup>3</sup> High Magnetic Field Laboratory, Institute of Plasma Physics, Chinese Academy of Sciences, Hefei 230031, People's Republic of China

E-mail: zhwang@netra.nju.edu.cn

Received 24 August 2001, in final form 14 January 2002

Published 22 February 2002

Online at [stacks.iop.org/SUST/15/586](http://stacks.iop.org/SUST/15/586)

## Abstract

We have measured the temperature dependence of top and bottom voltage signals of a  $Y_{0.8}Er_{0.2}Ba_2Cu_3O_{7-\delta}$  crystal in magnetic field up to 7.5 T parallel to the  $c$ -axis using the pseudo-flux-transformer method. The results show that in a dissipative regime the voltage signal on the side of the applied current contacts is more than that on the opposite side; meanwhile the bottom voltage signal shows a field-dependent peak effect near the critical temperature  $T_c$ . We calculated the true resistivities  $\rho_{ab}$  and  $\rho_c$  of the crystal within an anisotropic model. The difference between the calculated  $\rho_{ab}$  and  $\rho_c$  and the experimental values  $\rho_{ab}^{st}$  and  $\rho_c^{st}$  is helpful in understanding flux dynamic behaviour. Based on the Yeshurun–Malozemoff model, we have investigated temperature and field dependences of effective activation energy along the  $ab$ -plane and  $c$ -axis obtained from the  $\rho_{ab}(T)$  and  $\rho_c(T)$ , respectively. The temperature dependence of effective activation energy along the  $c$ -axis displays a good thermally activated flux flow (TAFF) behaviour. In the TAFF regime the field dependence of effective activation energy follows a power behaviour,  $U(H) = 4.24 \times 10^4 H^{-1.1}$ . The TAFF regime and the coupling between the layers have been discussed.

## 1. Introduction

It is well known that the Y-based cuprate superconductor has a layered, oxygen-deficient perovskite structure. Such layered structure results in a very strong anisotropic behaviour of normal and superconducting properties. The  $ab$ -plane and  $c$ -axis resistivities and the superconducting coupling between  $CuO_2$  planes are essential for a complete understanding of the dissipation mechanism of the high- $T_c$  superconductors (HTSCs). Generally, the  $ab$ -plane dissipative mechanism is easily understood by the thermally activated flux flow in the presence of an applied magnetic field [1–3]. However, the dissipative mechanism of out-of-plane resistivity has been a controversial issue [4]. For temperature dependence of

$c$ -axis resistivity, the behaviour of metals and semiconductors have been reported by many papers as seen in [5]. Since a much shorter coherence length  $\xi$  and much higher thermal energy  $k_B T$  exists near the superconducting transition in HTSCs than that found in conventional superconductors, thermally activated flux motion and coupling between superconducting layers play an important role during the onset of finite resistance. Although Anderson [6] has pointed out that  $c$ -axis coupling is the motivation for superconductivity, there is still uncertainty about the dissipation mechanism of the out-of-plane resistivity.

The dc flux transformer configuration is an appropriate method of exploring the intrinsic resistivity of HTSCs. Eltsev and Rapp [7] and Doyle *et al* [8] have successfully explained

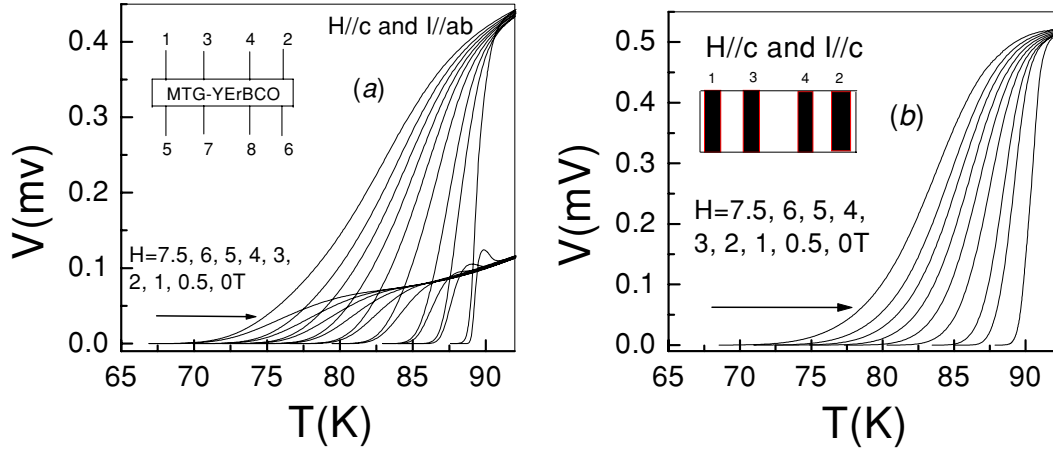


**Figure 1.** (a) Temperature dependence of top and bottom voltage signals ( $V_{34}$  and  $V_{78}$  with  $I_{12}$ ) for a MTG- $Y_{0.8}Er_{0.2}Ba_2Cu_3O_{7-\delta}$  crystal at magnetic fields up to 7.5 T for  $H//c$  with  $H \perp J$ . Inset displays the contact configuration. (b) Temperature dependence of voltage signal  $V_{37}$  with  $I_{15}$  at magnetic fields up to 7.5 T for  $H//c$  with  $H \perp J$ . The inset shows the shape of silver contacts on the top surface of the crystal.

their transformer measurements using a local anisotropic electrodynamic scenario only and compared their results with directly measured  $\rho_c$  data. The interpretation of flux transformer data hinges on the temperature dependence of the resistivity in the  $ab$ -plane  $\rho_{ab}$  and  $c$ -axis  $\rho_c$ . To understand the superconducting and dissipative mechanisms in an Er-doping MTG-YBCO crystal, we have measured the top and bottom resistivities,  $R_{top}$  and  $R_{bot}$ , and the  $c$ -axis resistivity  $R_c$  as a function of temperature  $T$  using a transformer configuration at various magnetic fields up to 7.5 T parallel to the  $c$ -axis. The aim of our study is to explore the origin of the dissipative resistivities  $\rho_{ab}$  and  $\rho_c$  in the applied magnetic field and discuss whether the vortices in the superconductor move as three-dimensional entities in the form of flux tubes or incoherently as two-dimensional objects within the  $CuO_2$  planes.

## 2. Sample and experiment

The Er-doped YBCO ( $Y_{0.8}Er_{0.2}Ba_2Cu_3O_{7-\delta}$  + 40% mol  $Y_2BaCuO(211)$ ) crystal used in this study was prepared by the melted-textured-growth method. The detailed process and quality of the crystals were reported in [9]. A crystal with size  $8.7 \times 4.7 \times 0.5$  mm<sup>3</sup> cut from these single bulks was held on a rotatable sample holder, where the angle between the applied magnetic field  $H$  and surface of the film could be adjusted conveniently and the resolution of the angle was  $0.1^\circ$ . Contacts were made by vacuum evaporation of silver films and soldering of silver wires to them, as shown in the inset of figure 1(a). Typical contact resistance was less than  $0.5 \Omega$ . The resistance was measured by flux transformer configuration, as shown in the inset of figure 1(b), using the method of plus and minus current. A programmable Keithley 220 current supplier was used as the current source. Two Keithley 182 nanovoltmeters were used to detect the top and bottom voltage signals with a resolution of 2 nV. A magnetic field up to 8 T was supplied by a superconducting solenoid magnet system. The temperature was measured by a calibrated Rh-Fe resistance thermometer and corrected for the effect of magnetic field. The zero resistance temperature of the sample is 87.7 K and the magnetic critical current density  $J_c$  is  $2.4 \times 10^4$  A cm<sup>-2</sup> at 77.3 K in zero magnetic field.

Before discussing the experimental data, we have to define the notations. As shown in the inset of figure 1(b), while measuring current  $I$  was injected from electrode 1 to 2, the voltage signal on the top surface over contacts 3 and 4 (denoted as  $V_{34}$ ) is called  $V_{top}$ , and the voltage signal on the bottom surface over contacts 7 and 8 (denoted as  $V_{78}$ ) is called  $V_{bot}$ . The  $SV_{top}/Il$  and  $SV_{bot}/Il$  were defined as  $\rho_{top}$  (or called  $\rho_{ab}^{st}$  later) and  $\rho_{bot}$ , respectively, where  $l$  is the distance between the voltage contacts,  $S$  is the area of cross section. When current is injected through contacts 1 and 5, then the voltage signal between contacts 3 and 7 ( $V_{37}$ ) will be called  $V_c$ ,  $S'V_c/ID$  is defined as  $\rho_c^{st}$ , where  $D$  is the thickness of the crystal and  $S'$  is the area of the crystal top or bottom surface. The true resistivities  $\rho_{ab}$  and  $\rho_c$  are calculated from the experimental data as in equations (5(a)–(b)).

## 3. Results and discussion

Figure 1(a) shows the typical temperature dependence of top and bottom voltage signals ( $V_{top}$  and  $V_{bot}$ ) in the applied magnetic field up to 7.5 T parallel to the  $c$ -axis for the MTG-YErBCO crystal. Both top and bottom voltages were simultaneously measured at the same temperature using measuring current  $I = 50$  mA corresponding to the current density of  $2$  A cm<sup>-2</sup>. The result of figure 1(a) can be summarized as follows: (1) at zero field, the transition is sharp and has a zero resistance temperature  $T_{c0}$  87.66 K; (2) resistive transition in the presence of the magnetic field exhibits a broadening induced by the magnetic field; (3)  $V_{top} > V_{bot}$  in the resistive transition regime and (4) there is peak effect near the critical temperature in the  $V_{bot}(T)$  curve and the peak is depressed by the applied magnetic field. This behaviour is quite different from the results obtained by Safar *et al* [10] and Eltsev *et al* [7] in YBCO single crystal, and Safar *et al* [11] and Busch *et al* [12] in Bi-2212 single crystals using the same measuring method. We cannot observe temperature where  $V_{top} = V_{bot}$  in the crystal. To explore the origin of  $V_{top} > V_{bot}$  and the peak in the  $V_{bot}(T)$  curve, we have also measured the temperature dependence of voltage between contacts 3 and 7 ( $V_{37}$ ) when measuring current  $I$  is injected from contact 1 to 5 ( $I_{15}$ ), as shown in figure 1(b). The resistive transition shows

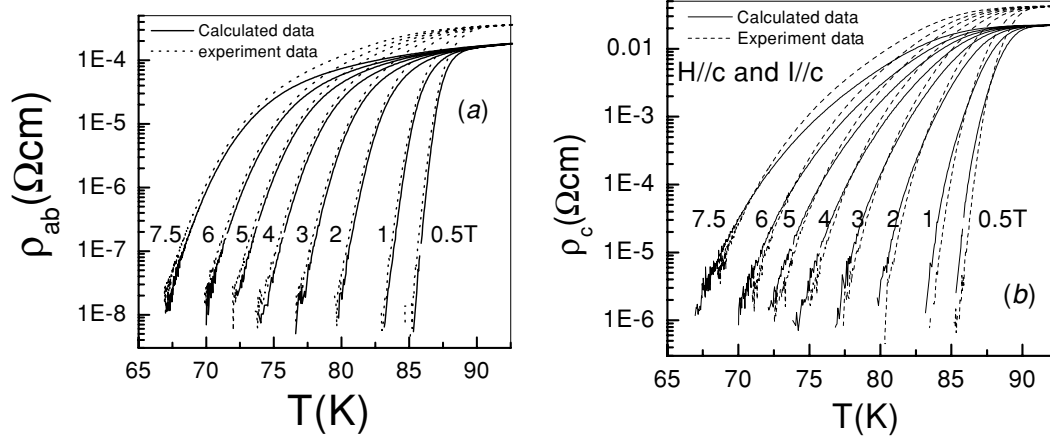


**Figure 2.** (a) Temperature dependence of  $\rho_{\text{top}}$  ( $V_{34}S/Il$ ) (dashed lines) and  $\rho_{ab}$  (solid lines) at various magnetic fields for  $H//c$ . (b) Temperature dependence of  $\rho_c^{st}$  ( $V_{37}S'/I_{15}D$ ) (dashed lines) and  $\rho_c$  (solid lines) at various magnetic fields for  $H//c$ .

a semiconductor behaviour above the critical temperature  $T_c$ , and a broadening induced by the magnetic field below  $T_c$ . A similar result has been reported in [2].

In order to understand our results, we take into account the non-uniform current distribution and proceed with a linear anisotropy model [12]. Due to the current contact arrangement, as shown in the inset of figure 1(a), current density distribution in  $y$ -axis can be neglected and we take the two-dimensional potential distribution  $V(x, z)$  in the following form:

$$\nabla \cdot \mathbf{j} = \frac{1}{\rho_{ab}} \frac{d^2 V}{dx^2} + \frac{1}{\rho_c} \frac{d^2 V}{dz^2} = 0. \quad (1)$$

An appropriate solution is given by an expansion [12]

$$V(x, z) = \sum V_n \sin\left(\frac{n\pi x}{a}\right) \cosh\left[\left(\frac{\rho_c}{\rho_{ab}}\right)^{1/2} \frac{n\pi z}{a}\right] \quad (2)$$

$n = 1, 3, 5, \dots$

where  $a$  is the length of the sample along the direction of transport current. The solution should satisfy the surface boundary condition of current density,  $j_z = 0$  at the bottom of  $z = 0$  and  $j_x = 0$  at both the edges where  $x = \pm a/2$ . According to the symmetry in the  $x$ -direction, it is satisfied that the normal component  $j_z$  is zero at the midpoint of both current contact pads. We may approximate  $V(x, z)$  by the lowest  $n = 1$  alone. Since there is no normal component at the midpoint where  $x = 0$ , the applied current  $I$  must be equal to the integrated current density along the  $x$ -axis, that is

$$I = b \int j_x dz \quad (3a)$$

where  $b$  is the width of the crystal in  $y$ -direction. Thus  $V_i$  is uniquely determined and  $V(x, z)$  can be written as

$$V(x, z) \approx -\frac{I}{b} (\rho_c \rho_{ab})^{1/2} \frac{\sin\left(\frac{n\pi x}{a}\right)}{\sinh\left[\left(\frac{\pi D}{a}\right) (\rho_c \rho_{ab})^{1/2}\right]} \times \cosh\left[\frac{\pi}{a} \left(\frac{\rho_c}{\rho_{ab}}\right)^{1/2} z\right]. \quad (3b)$$

Corresponding equation (3) at  $(x_i, z = D, i = 3, 4)$  and  $(x_i, z = 0, i = 7, 8)$  with the experimental results  $V_{\text{top}}$  and  $V_{\text{bot}}$ ,

we get the following equations:

$$V_{\text{top}} \approx -\frac{I}{b} (\rho_c \rho_{ab})^{1/2} \frac{\sin\left(\frac{n\pi x_1}{a}\right) - \sin\left(\frac{n\pi x_2}{a}\right)}{\sinh\left[\left(\frac{\pi D}{a}\right) (\rho_c \rho_{ab})^{1/2}\right]} \times \cosh\left[\frac{\pi}{a} \left(\frac{\rho_c}{\rho_{ab}}\right)^{1/2} z\right] \quad (4a)$$

and

$$V_{\text{bot}} \approx -\frac{I}{b} (\rho_c \rho_{ab})^{1/2} \frac{\sin\left(\frac{n\pi x_1}{a}\right) - \sin\left(\frac{n\pi x_2}{a}\right)}{\sinh\left[\left(\frac{\pi D}{a}\right) (\rho_c \rho_{ab})^{1/2}\right]}. \quad (4b)$$

To take into account the symmetric distribution of both voltage pods, we regard the contact point  $x_2 = -x_1 = x_0 \approx a/6$ . Therefore, according to equations 4(a) and 4(b), the 'true' resistivities  $\rho_{ab}$  and  $\rho_c$  can be obtained as the following forms:

$$\rho_{ab} \approx \frac{\pi D}{a} \frac{V_{\text{top}} b}{2I \sin\left(\frac{\pi x_0}{a}\right)} \frac{\tanh\left[\text{arccosh}\left(\frac{V_{\text{top}}}{V_{\text{bot}}}\right)\right]}{\text{arccosh}\left(\frac{V_{\text{top}}}{V_{\text{bot}}}\right)} \quad (5a)$$

and

$$\rho_c \approx \frac{a}{\pi D} \frac{V_{\text{top}} b}{2I \sin\left(\frac{\pi x_0}{a}\right)} \tanh\left[\text{arccosh}\left(\frac{V_{\text{top}}}{V_{\text{bot}}}\right)\right] \times \text{arccosh}\left(\frac{V_{\text{top}}}{V_{\text{bot}}}\right). \quad (5b)$$

Figure 2 shows the temperature dependence of the calculated resistivities  $\rho_{ab}$  and  $\rho_c$ , respectively, in various applied magnetic fields, as shown by solid lines; while the temperature dependence of the experimental resistivities  $\rho_{ab}^{st}$  (or  $\rho_{\text{top}}$ ) and  $\rho_c^{st}$  is shown by dashed lines. The resistivities at 92.5 K are  $\rho_n(c) \approx 2.2 \times 10^{-2} \Omega \text{ cm}$  and  $\rho_n(ab) \approx 1.7 \times 10^{-4} \Omega \text{ cm}$ . The resistivity anisotropy is consistent with the effective mass anisotropy,  $\gamma = \frac{\xi_{ab}}{\xi_c} = \frac{\lambda_c}{\lambda_{ab}} = \sqrt{\frac{m_c}{m_{ab}}} = \sqrt{\frac{\rho_c}{\rho_{ab}}} \approx 11$ , obtained from the anisotropy of the superconducting property [9]. From figure 2, it is obviously seen that the value of  $\rho_{ab}(T)$  or  $\rho_c(T)$  is smaller than the value of  $\rho_{ab}^{st}$  or  $\rho_c^{st}$  deduced from  $SV_{\text{top}}/Il$  or  $S'V_c/ID$  in the whole experimental temperature region and there is no peak effect or abnormal behaviour in the  $\rho_{ab}(T)$  or  $\rho_c(T)$  curves. This phenomenon can be explained because our current contacts

are only in contact with the top of the sample and the current distribution in the crystal will be very inhomogeneous and confined to a thin top surface layer due to strongly anisotropic resistivity in this system. Thus it is evident that the ‘true’ resistivities  $\rho_{ab}$  and  $\rho_c$  parallel and perpendicular to the  $ab$ -plane cannot be obtained directly from simple division of the measured voltage and current.

It is well known that the thermally activated flux creep can produce dissipation suggested by Palstra *et al* [13] as follows:

$$\rho(T, H) = \rho_0 \exp(-U_0/\kappa_B T) \quad (6)$$

where  $\rho_0$  is the pre-exponential factor independent of field and orientation,  $\kappa_B$  is the Boltzman constant and  $U_0$  is the actual activation energy that generally depends on temperature  $T$ , current density  $J$  and applied magnetic field  $H$ . Generally, the current density dependence of activation energy is a constant when the measuring current density is lower than  $10^3$  A cm<sup>-2</sup> [14, 15].

From equation (6), we can understand that the slope ( $-\text{d}(\ln\rho)/\text{d}(1/T)$ ) of the Arrhenius plot is the actual effective activation energy  $U_{\text{eff}} = U_0$ . Therefore, we can get information about the temperature dependence of the actual activation energy  $U_{\text{eff}}$  from the temperature dependence of  $-\text{d}(\ln\rho)/\text{d}(1/T)$ . Figure 3 shows the temperature dependences of  $-\text{d}(\ln\rho_{ab})/\text{d}(1/T)$ ,  $-\text{d}(\ln\rho_c)/\text{d}(1/T)$  and  $-\text{d}(\ln\rho_c^{\text{st}})/\text{d}(1/T)$ , respectively, at various magnetic fields for  $H//c$ . We can find that the slope increases rapidly with decrease in temperature, the temperature dependence of the slope  $-\text{d}(\ln\rho_{ab})/\text{d}(1/T)$  shows an upward curvature in the dissipative regime at a fixed field. However, the temperature dependence of the slope  $-\text{d}(\ln\rho_c)/\text{d}(1/T)$  and/or  $-\text{d}(\ln\rho_c^{\text{st}})/\text{d}(1/T)$  shows a similar behaviour: a downward curvature above a certain temperature  $T^*$  and an upward curvature below  $T^*$  at a fixed field. A similar phenomenon has been observed by Kim *et al* [16] in HgBCCO thin film and Safar *et al* [17] in BSCCO-2212 single crystals. Below  $T^*$ , the effective activation energy increases rapidly with a decrease in temperature. Safar *et al* [17] and Carruzzo and Yu [18] claimed that the rapid increasing of effective energy with the decreasing temperature shows the vortex lines in a vortex-glass state. According to the results reported by Kim *et al* [16], we consider that the downward curvature of  $-\text{d}(\ln\rho_c)/\text{d}(1/T)$  versus  $T$  curve might indicate that the vortex lines are in the TAFF region above temperature  $T^*$ . The description of TAFF behaviour is given in the following. Nevertheless, in figure 3(a) the temperature dependence of the effective activation energy can be described as a linear behaviour in the low-temperature part, as shown by the dashed lines. That is to say, the effective activation energy  $U_{\text{eff}}$  follows a linear equation of temperature. The slope of  $U_{\text{eff}}(T)$  decreases with the increasing applied magnetic field.

Considering the field and temperature dependences of activation energy  $U_0$  in equation (6) at a constant measuring current density, we can write the activation energy as  $U_0(H, T) = U(H)U(T) = U(H)(1 - T/T_c)^b$ . Therefore, we can obtain the effective activation energy

$$\begin{aligned} U_{\text{eff}} &= -(\text{d}\ln\rho)/\text{d}(1/T) = U_0 - T \text{d}U_0/\text{d}T \\ &= U(H)(1 - T/T_c)^b [1 + b(T/T_c)/(1 - T/T_c)]. \end{aligned} \quad (7)$$

If we accept the temperature dependence of activation energy,  $U(T) = (1 - T/T_c)^b$  with  $b = 3/2$ , suggested by

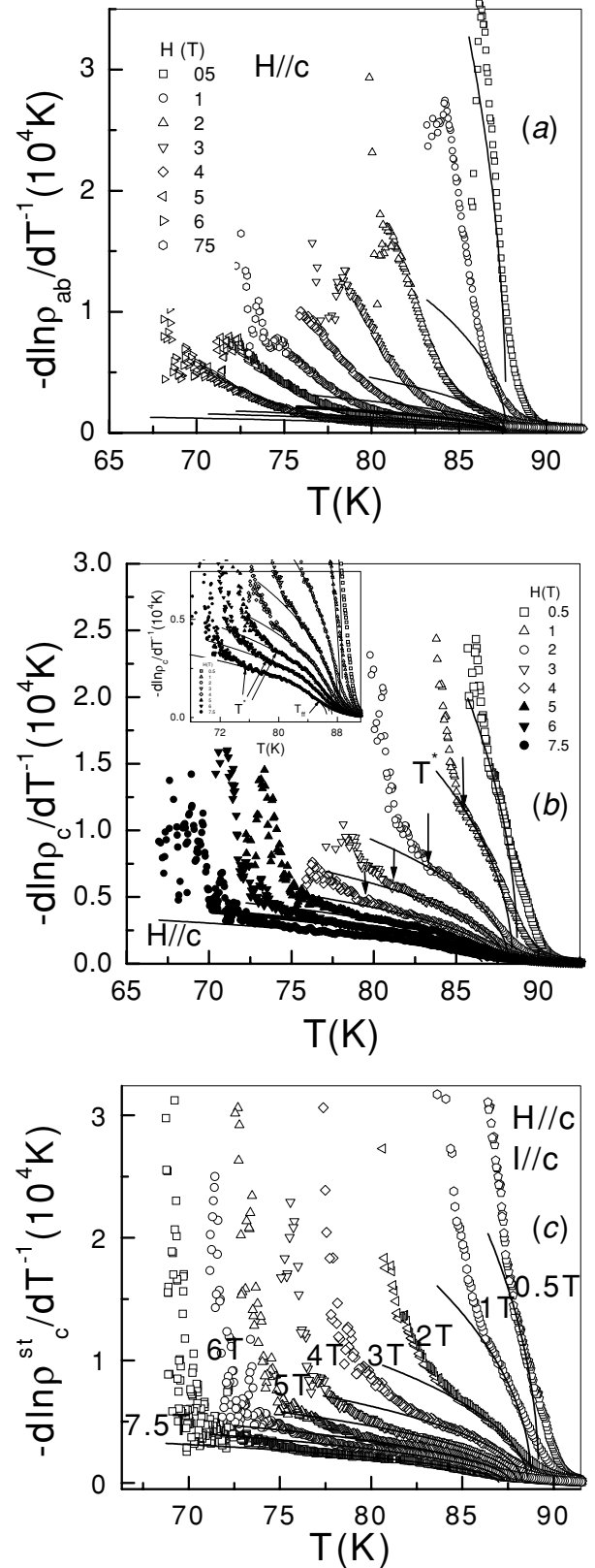


**Figure 3.** (a) Temperature dependence of effective activation energy at various magnetic fields for  $H//c$ . The data of figures 3(a)–(c) are deduced from  $\rho_{ab}(T)$  in figure 2(a),  $\rho_c(T)$  (solid line in figure 2(b)) and  $\rho_c^{\text{st}}(T)$  (dashed line in figure 2(b)), respectively. The solid line is calculated by equation,  $U_e(T, H) = U(H)(1 - T/T_c)^{3/2} [1 + 1.5T/(T_c - T)]$ , for different magnetic fields. (b) The inset of figure 3(b) shows the enlarged TAFF regime for higher magnetic field.

Yeshurun and Malozemoff [19] in the TAFF region, the effective activation energy should be followed in the form

$$U_{\text{eff}} = U(H) \left(1 - \frac{T}{T_c}\right)^{3/2} \left[1 + \frac{3T}{2(T_c - T)}\right]. \quad (8)$$

There are two fitting parameters  $U(H)$  and  $T_c$  in equation (6). In order to scale the temperature dependence of the actual activation energy in TAFF regime, the fitting parameters  $U(H)$  and  $T_c$  have been chosen for several times. The fitting parameters  $U(H)$  and  $T_c$  depend on the applied magnetic field  $H$ . The solid lines presented in figure 3 are the temperature dependences of the effective activation energy  $U_{\text{eff}}$  calculated by equation (8). From figure 3(a), we cannot see a TAFF regime in the  $ab$ -plane. This result might infer that there is a two-order phase transition induced by a number of disorders, such as twinned boundary and Er-doping cell, in the crystal. However, the temperature dependence of the effective activation energy deduced from  $\rho_c(T)$  shows a TAFF regime above  $T^*$ . To observe the TAFF regime clearly, the temperature dependence of the effective activation energy has been replotted, as shown in the inset of figure 3(b). In addition, near the critical temperature there is another deviation of the experimental data from the theoretical curve at a constant magnetic field. In general, the deviation is considered as the boundary between the TAFF and the flux flow regions where the temperature was symbolized as  $T_{\text{ff}}$  in the figure 3(b). At  $T_{\text{ff}}$  the activation energy starts to become comparable to the thermal  $T$ . Above  $T_{\text{ff}}$ , the flux lines are in the free flow region. As seen in the figures 3(b) and 3(c), the  $\rho_c^{\text{st}}$  and  $\rho_c$  can be fitted well with Yeshurun and Malozemoff model.

Figure 4(a) gives the field dependence of the fitting parameter  $U(H)$  whereas figures 3(b) and 3(c) give for  $H//c$ . From the figure 4(a), the magnitude of the effective energy  $U$  for the YErBaCuO crystal is around from  $4.7 \times 10^3$  K at 7.5 T to  $8.3 \times 10^4$  K at 0.5 T for  $H//c$ , a little less than that for YBCO [13]. The value of  $U(H)$  decreases with the increasing applied magnetic field and follows a power-law behaviour,  $U = AH^{-\alpha}$  with  $A = 4.24 \times 10^4$  K and  $\alpha = 1.1$ . The dashed line in the figure 4(a) is a fitting line. This result indicates the consistency of  $\rho_c^{\text{st}}$  and  $\rho_c$ . As reported by Yeshurun and Malozemoff [19],  $\alpha = 1.1$  indicates that the extrinsic point pinning is the main flux pinning. The extrinsic point pinning might have resulted from the Er addition.

The field dependence of the characteristic temperature  $T^*$ ,  $T_{\text{ff}}$ , the irreversibility temperature  $T_{\text{irr}}$  determined by  $R/R_n = 0.05\%$  and the fitting parameter  $T_c$  for  $H//c$  can be drawn in a picture, as shown by the solid symbols in figure 4(b).  $T_{\text{irr}}(H)$ ,  $T^*(H)$ ,  $T_{\text{ff}}(H)$  and  $T_c$  follow the same behaviour  $H \propto (1 - T)^n$  with different  $n = 1.34, 1.29, 1.17$  and  $1.0$ , respectively. From figure 4(b), we can see that the phase diagram of Er-doped MTG-YBCO crystal is separated into several regions, namely flux flow, TAFF, flux softened and vortex solid regions by three lines of  $H - T_{\text{ff}}$ ,  $H - T^*$  and  $H - T_{\text{irr}}$ . At a fixed magnetic field, when the temperature decreases from above  $T_c$ , the vortex lines firstly undergo a transition from flux flow to thermally activated flux flow. As the temperature decreases further, the flux lines go through a transition from thermally activated flux flow to the vortex glass. In the vortex glass, the vortex lines are softening and the activation energy increases rapidly with the decreasing temperature. Finally, the vortex lines go

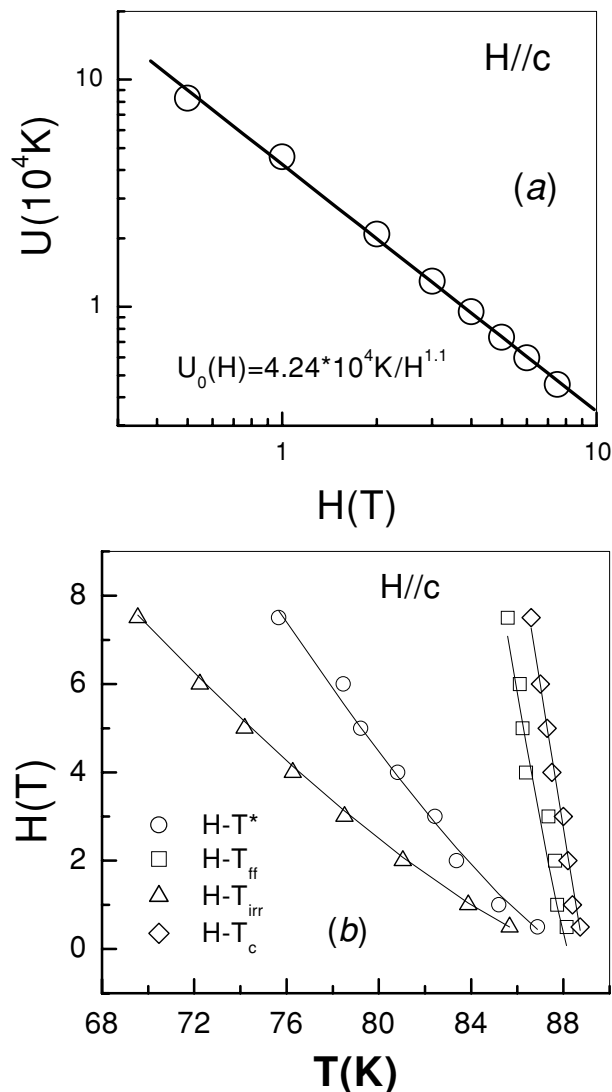


**Figure 4.** (a) Field dependence of the fitting parameter  $U_0(H)$  for  $\rho_c(T)$  and  $\rho_c^{\text{st}}(T)$ . The dashed line is the fitting curve,  $U_0(H) = 4.24 \times 10^4 H^{-1.1}$ . (b) Field dependence of temperatures  $T^*$ ,  $T_{\text{ff}}$ ,  $T_{\text{irr}}$  and  $T_c$  obtained from  $\rho_c$ . The solid lines are the fitting curves.

into the solid region below the irreversibility temperature,  $T_{\text{irr}}$ . The existence of the flux-softened region might indicate that the melting transition of flux lines is a second-order phase transition [18, 20] in our sample with correlated disordered defects.

#### 4. Conclusions

Using the dc flux transformer we have measured the temperature dependence of the top and bottom voltage signals and of  $c$ -axis resistivity  $\rho_c^{\text{st}}$  in a MTG-YErBCO single crystal. We obtained the ‘true’ resistivity  $\rho_{ab}$  and  $\rho_c$  within a linear anisotropy model. We find that the true resistivity  $\rho_c(T)$  shows a good TAFF behaviour. In the TAFF regime the field dependence of the effective activation energy follows a power behaviour,  $U(H) = 4.24 \times 10^4 H^{-1.1}$ . The peak effect of a bottom voltage signal can be described by a uniform distribution of measuring current in the sample volume.

The phase diagram of a Er-doped MTG-YBCO crystal can be separated into four regions, namely flux flow, TAFF, soft vortex glass and vortex solid regions by three lines of  $H - T_{\text{ff}}$ ,  $H - T^*$  and  $H - T_{\text{irr}}$ .

### Acknowledgments

This study is supported by the National Natural Science Foundation of China (NNSFC-10174033), the Ministry of Science and Technology of China (NKBR SF-G19990646) and the Nanjing University Talent Development Foundation.

### References

- [1] Blatter G, Feigel'man M V, Geshkenbein V B, Larkin A L and Vinokur V M 1994 *Rev. Mod. Phys.* **66** 1125
- [2] Brandt E H 1995 *Rep. Prog. Phys.* **58** 1465
- [3] Cohen L F and Jensen H J 1997 *Rep. Prog. Phys.* **60** 1581
- [4] Kadowaki K, Songliu Y and Kitazawa K 1994 *Supercond. Sci. Technol.* **7** 519
- [5] Iye Yasuhiro 1992 *Physical Properties of High Temperature Superconductors* vol 3 ed Donald M Ginsberg (Singapore: World Scientific) p 285
- [6] Anderson P W 1998 *Science* **279** 1196
- [7] Eltsev Y, Holm W and Rapp O 1994 *Phys. Rev. B* **51** 9419
- [8] Doyle R A, Seow W S, Yan Y, Campbell A M, Mochiku T, Kadowaki K and Wirth G 1996 *Phys. Rev. Lett.* **77** 1155
- [9] Wang Z H, Zou X W, Fang J, Yang T, Tang Y L, Huang Z, Qiu L, Chen J L, Zhang H and Ding S Y 2002 *Supercond. Sci. Technol.* **15** 183
- [10] Safar H, Gammel P L, Huse D A, Majumdar S N, Schneemeyer L F and Bishop D J 1994 *Phys. Rev. Lett.* **72** 1272
- [11] Safar H *et al* 1992 *Phys. Rev. B* **46** 14238
- [12] Busch R, Ries G, Werthner H, Kreiselmeier G and Saemann-Ischenko G 1992 *Phys. Rev. Lett.* **69** 522
- [13] Palstra T T M, Batlogg B, van Dover R B, Schneemeyer L F and Waszczak J V 1990 *Phys. Rev. B* **42** 6621
- [14] Wang Z H and Cao X W 1999 *Solid State Commun.* **109** 709
- [15] Wang Z H 1999 *Supercond. Sci. Technol.* **12** 421
- [16] Kim Wan-seon, Kang W N, Kim Mun-Seog and Lee Sung-Ik 2000 *Phys. Rev. B* **61** 317
- [17] Safar H, Gammel P L, Bishop D J, Mitzi D B and Kapitulnik A 1992 *Phys. Rev. Lett.* **68** 2672
- [18] Carruzzo H M and Yu C C 1998 *Phil. Mag. B* **77** 1001
- [19] Yeshurun Y and Malozemoff A P 1988 *Phys. Rev. Lett.* **60** 2202
- [20] Fisher D S, Fisher M P A and Huse D A 1991 *Phys. Rev. B* **43** 130